

Quantitative study on anomalous Nernst effect in Co thin films by laser irradiation

Soichiro Mochizuki,¹ Itaru Sugiura,² Tetsuya Narushima,¹ Teruo Ono,^{2,3}

Takuya Satoh,¹ and Kihiro T. Yamada^{1,*}

¹*Department of Physics, Institute of Science Tokyo, Tokyo 152-8551, Japan*

²*Institute for Chemical Research, Kyoto University, Uji, Kyoto 611-0011, Japan*

³*Center for Spintronics Research Network, Institute for Chemical Research, Kyoto University, Uji, Kyoto, 611-0011, Japan*

*Corresponding author: yamada@phys.sci.isct.ac.jp

Abstract

The anomalous Nernst effect (ANE) generates electromotive forces transverse to temperature gradients and has attracted much attention for potential applications into novel thermoelectric power generators. ANE efficiency is generally characterized by uniform temperature gradients in a steady state prepared by heaters. However, although focusing laser beams on a magnetic film can form much larger temperature gradients, the laser irradiation method has not been sufficiently considered for quantifying the ANE coefficient due to the difficulty in estimating the localized in-homogeneous temperature gradients. In this study, we present a quantitative study of ANE in Ru(5 nm)/Co(t_{Co}) (t_{Co} = 3, 5, 7, 10, 20, 40, and 60 nm) bilayers on sapphire (0001) substrates by combining a laser irradiation approach with finite element analysis of temperature gradients under laser excitation. We find that the estimated ANE coefficients are consistent with previously reported values and one independently characterized using a heater. Our results also reveal the advantages of the laser irradiation method over the conventional method using heaters. Intensity-modulated laser beams can create ac temperature gradients as large as approximately 10^3 K/mm at a frequency of tens of kilohertz in a micrometer-scale region.

I. INTRODUCTION

Spin caloritronics [1,2], which studies the spin transport properties driven by heat currents in magnetic materials, has developed rapidly since the discovery of the spin Seebeck effect [3]. The anomalous Nernst effect (ANE) [4] generates electromotive forces (\mathbf{E}_{ANE}) in a cross-product direction of magnetization (\mathbf{M}) and temperature gradient (∇T) as follows:

$$\mathbf{E}_{\text{ANE}} = Q_{\text{ANE}} (4\pi\mathbf{M} \times \nabla T), \quad (1)$$

where Q_{ANE} is the ANE coefficient. While Seebeck generators produce electromotive forces in the same direction as ∇T , the \mathbf{E}_{ANE} is generated orthogonal to the ∇T . This transverse configuration can be used to fabricate thin flexible thermoelectric power generators. However, their thermoelectric conversion efficiencies are insufficiently high for practical power generators. To increase conversion efficiency, material developments recently have focused on magnetic alloys, magnetic hybrid structures, and topological magnets [5–17].

Uniform temperature gradients prepared using heaters are generally used to study the ANE and the spin Seebeck effect [18–21]. By contrast, temperature gradients can be formed using laser absorption. The temperature gradients formed using laser irradiation are localized, which enables visualization of the local magnetization direction by measuring the generated electric voltages [22–28]. Moreover, because visible laser beams exponentially decay by tens of nanometers inside a metallic film, the temperature gradient should be enormous compared to when a temperature difference is prepared using heaters across a sub-millimeter-thick substrate. However, the difficulty in estimating temperature gradients under laser excitation has impeded its active use in evaluating Q_{ANE} .

In this study, we present a quantitative study of the ANE in Co thin films using laser irradiation. Because the laser absorption profile is sensitive to film thicknesses of tens of nanometers, we exploited the Co thickness of Q_{ANE} to ascertain the applicability of the laser irradiation method. To estimate the Q_{ANE} values, the transverse electric voltages were measured when the magnetic film was excited by intensity-modulated laser beams. Finite element simulations enabled us to analyze the spatial profiles of the light electric field and the temperature inside the Co film. We find a quantitative and qualitative agreement of the Q_{ANE} values with previously reported values and our value characterized using a heater. Furthermore, our results reveal the multiple merits of the laser irradiation method compared to the conventional method of using heaters.

II. METHODS

A. Experimental configuration

We deposited bilayers consisting of Ru(5 nm)/Co(t_{Co}) ($t_{\text{Co}} = 3, 5, 7, 10, 20, 40, \text{ and } 60 \text{ nm}$) on *c*-plane sapphire substrates by dc sputtering. The Ru layer was selected owing to its tolerance to oxidization. By standard photolithography techniques, the bilayers were processed to a Hall cross of (w, l) = (0.40

mm, 0.40 mm), where w and l denote the width and length of the Hall cross, respectively. Electrical contacts consisting of Au(20 nm)/Cu(80 nm)/Ti(5 nm) by rf sputtering. The electrical contacts were connected with gold wires using a wire bonder.

Figure 1 shows a schematic of the experimental setup. A diode-pumped solid-state green laser with a wavelength of $\lambda = 532$ nm was used for the small beam divergence angle. The laser intensity was modulated stably using the optics shown in Fig. 1. Linearly polarized laser beam with a polarization angle of $+45^\circ$ from a Glan Taylor prism propagates into a photo-elastic modulator (PEM) which was set to give a retardation of $\gamma = \gamma_0 \sin \Omega t$ to the X -polarized component. The polarization-modulated laser beam passed through a half-wave plate, of which the fast axis was rotated by $+22.5^\circ$ from the X -axis. Then, the Y -polarized component was then extracted using another Glan Taylor prism. In this current configuration, the polarization state of the laser output is described using the Jones vector, as follows [29]:

$$\mathbf{e} = \begin{pmatrix} 0 & 0 \\ 0 & 1 \end{pmatrix} \frac{1}{\sqrt{2}} \begin{pmatrix} 1 & 1 \\ 1 & -1 \end{pmatrix} \begin{pmatrix} e^{i\gamma} & 0 \\ 0 & 1 \end{pmatrix} \frac{1}{\sqrt{2}} \begin{pmatrix} 1 \\ 1 \end{pmatrix} = \frac{1}{2} \begin{pmatrix} 0 \\ e^{i\gamma} - 1 \end{pmatrix}. \quad (2)$$

Using Bessel functions of the first kind for n^{th} integer orders, $J_n(\gamma_0)$, the intensity of the output, I_{out} , is expressed as follows:

$$\begin{aligned} I_{\text{out}} &= \mathbf{e}^* \cdot \mathbf{e} = \frac{1}{2} - \frac{1}{2} \cos(\gamma_0 \sin \Omega t) \\ &= \frac{1}{2} - \frac{1}{2} [J_0(\gamma_0) + 2J_2(\gamma_0) \cos 2\Omega t + J_4(\gamma_0) \cos 4\Omega t + \dots]. \end{aligned} \quad (3)$$

The retardation of the PEM was set at $\gamma_0 = \pi$. In this case, I_{out} becomes

$$I_{\text{out}} = 0.6521 - 0.4854 \cos 2\Omega t - 0.1514 \cos 4\Omega t + \dots \quad (4)$$

The intensity ratio of the dc, 2Ω , and 4Ω components is 1:0.744:0.232. For calibrating the PEM, we measured the dc and 2Ω voltages from a photodetector using a multimeter and a lock-in amplifier, respectively. The driving frequency of the PEM was fixed at $\Omega/2\pi = 42$ kHz. The intensity modulation method using a PEM is more accurate and stable than a mechanical method using an optical chopper. Using an objective lens with a magnification of $\times 2$, the laser output was focused on the right center of the Hall cross to maintain symmetric in-plane temperature gradients in space. We directly checked using a camera that the focused beam had a Gaussian intensity profile with a FWHM, $\alpha_{\text{FWHM}} = 30$ μm . The magnetization of Co was saturated in a direction titled by φ from the X -axis within the film plane using a magnetic field generated by an electromagnet mounted on a rotation stage. During the illumination of the laser beam, we measured 2Ω voltages between the counter electrodes using a lock-in amplifier.

B. Simulation condition

COMSOL Multiphysics 6.2 [30] was used to evaluate the temperature gradients inside the Co films

created by laser irradiation. The spatial profile of the light electric field was simulated using the Electromagnetic Waves, Beam Envelopes interfaces of the Wave Optics Module [31]. Moreover, the spatial temperature profile was simulated using the Heat Transfer in Solids interface of the Heat Transfer Module [32]. Figure 2 shows the simulation geometry composed of the sapphire substrate layer, Ru and Co layers, and air 1 and air 2 layers. Note that the definition of the coordinate system is changed in the following calculations: $\hat{x} \parallel \hat{X}, \hat{y} \parallel -\hat{Y}, \hat{z} \parallel -\hat{Z}$. For the constraints of the Wave Optics Module, we simulated the spatial profile of the light electric field in the substrate, Ru/Co, and air 1 layers. The spacious air 2 layer and the substrate layer act as heat bathes when calculating the spatial temperature profile. Using the geometrical condition of Fig. 2 and material parameters listed in Table 1, we simulated the spatial profiles of light electric field and temperature when Gaussian laser beam with $\alpha_{\text{FWHM}} = 30 \mu\text{m}$ and $\lambda = 532 \text{ nm}$ propagates from the air to metallic layers. Here, we used typical bulk values for the refractive indexes at $\lambda = 532 \text{ nm}$. The thermal conductivities of the Ru and Co films were estimated on the basis of their resistivities, as discussed later. We verified that the convergence and reliability did not change by further expanding the thicknesses of the air 2 and substrate layers. While the temperature profile of the substrate layer changes with a further increase in thickness, the temperature profile of the thin Co layer is hardly affected. Simulating the time evolution of the temperature profiles in three-dimensional space requires substantial computational cost and time. Therefore, we performed the simulation in a two-dimensional system, in which the y -width of the system was identical to twice the size of the standard deviation of the Gaussian laser beam $\sigma = \alpha_{\text{FWHM}} \sqrt{2/\ln 2}$.

III. RESULTS AND DISCUSSION

A. Magnetization, resistivity, and thermal conductivity

We characterized the t_{Co} dependence of the saturation magnetization, $4\pi M_s$, shown in Fig.3(a) using a superconducting quantum interference device and a vibrating-sample magnetometer. With increasing t_{Co} , $4\pi M_s$ approaches the bulk value of 18 kG [33]. The sheet resistances, R_s , of the fabricated devices, shown in Fig. 3(b) were measured using four-terminal sensing. The nonlinear t_{Co} dependence of R_s was used to estimate the resistivities of Ru (ρ_{Ru}) and Co (ρ_{Co}) layers. We assumed that the bilayer was equivalent to a parallel circuit consisting of the resistances of the Ru and Co layers, and the resistivities were constant in the Co and Ru thin films. Because the width and length of the Hall devices are equal, the sheet resistance is given by

$$R_s = \frac{\rho_{\text{Ru}}\rho_{\text{Co}}}{\rho_{\text{Ru}}t_{\text{Co}} + \rho_{\text{Co}}t_{\text{Ru}}}, \quad (5)$$

where the t_{Ru} is the Ru thickness of 5 nm. Fitting the t_{Co} dependence of the R_s shown in Fig. 3(b) with Eq. (5) gives $\rho_{\text{Ru}} = 5.2 \times 10^{-7} \Omega \text{ m}$ and $\rho_{\text{Co}} = 4.1 \times 10^{-7} \Omega \text{ m}$. Furthermore, by applying the Wiedemann-Franz law [34] to the resistivities, we obtain the thermal conductivities of the Ru and Co layers of $14.3 \text{ W m}^{-1}\text{K}^{-1}$ and $18.1 \text{ W m}^{-1}\text{K}^{-1}$, respectively. The calculated thermal conductivities are

comparable to previously-reported values of thin metals, including Co [35]. The estimated thermal conductivities were used in the simulations.

B. The anomalous Nernst effect induced by laser irradiation

Figure 4(a) shows the magnetic hysteresis of the electrical voltages (V) as a function of the magnetic field (H) at $\varphi = 90^\circ$ and an average laser power (P) of 70 mW for $t_{\text{Co}} = 10$ nm. This clear hysteresis indicates that the electromotive force reflects the magnetization of the Co layer. Furthermore, we define the voltage jump by magnetization reversals as $\Delta V = [V(H^+) - V(H^-)]/2$ at $H^\pm = \pm 800$ Oe. The measured φ dependence of ΔV for $t_{\text{Co}} = 10$ nm is shown in Fig. 4(b). For all the bilayers, the φ dependences of ΔV can be very well fitted with a sine function $\Delta V_{\text{fit}} \sin \varphi$. The values of ΔV_{fit} at $P = 70$ mW are plotted versus t_{Co} in Fig. 4(b). We observe a peak in the ΔV_{fit} at $t_{\text{Co}} = 7$ nm. Note that the ΔV linearly depends on P within the employed range of P at all the conditions of t_{Co} . For example, refer the case where $t_{\text{Co}} = 7$ nm [Fig. 4(d)].

C. Simulated spatial profiles of light electric fields and temperature

We simulated the spatial profiles of light electric field and temperature when the laser beam with $\lambda = 532$ nm propagates into the bilayer on the sapphire substrate. Figure 5(a) shows the spatial profiles of the light electric-field amplitude, $|\mathbf{E}|$, at $t_{\text{Co}} = 60$ nm. The laser beam was incident from air to the surface of the Ru layer. The light electric field is partially reflected at the interface between the air and Ru layers. Although the interference between the reflected and incident light generates standing light waves in the air layer, it does not change the amplitude of the transmitted light electric field. The transmitted-light electric field decays exponentially inside the metallic layers. The Wave Optics Module cannot handle pulsed and amplitude-modulated light electric fields. Instead, using the Heat Transfer Module, we introduced heat sources, of which the caloric generation oscillates at $2\Omega/2\pi$ while keeping the spatial profile of energy dissipation density (absorbed laser intensity). Because the following simulations considered only the laser power oscillating at $2\Omega/2\pi = 84$ kHz, the amplitude of the 2Ω component ($P_{2\Omega}$) of laser power is obtained by multiplying the P by a factor of 0.744.

Figure 5(b) shows the spatial temperature profile at $P_{2\Omega} = 52.1$ mW when the temperature change (ΔT) from the surface of the sapphire substrate is maximized. Furthermore, we defined a cut-line (broken line) along the center of the magnified view in Fig. 5(b) [Fig. 5(c)]. The temperatures along the cut-line change nonlinearly owing to the exponential decay of the light intensity [Fig. 5(d)]. Moreover, we evaluated the nonlinear temperature gradient by integrating the temperature gradients,

$$\theta = \int_{-(t_{\text{Ru}}+t_{\text{Co}})}^{-t_{\text{Ru}}} dz \nabla T(z),$$

which are divided by t_{Co} . We note that the feasible temperature gradients

can exceed 10^3 K mm^{-1} , which is two orders of magnitude larger than those when using heaters (~ 10 K mm^{-1}) [7,9,18,21,36]. The symmetric in-plane temperature gradient is approximately 5% of the

vertical temperature gradient. The ratio of the in-plane temperature gradient to the vertical temperature gradient did not significantly depend on t_{Co} . The laser intensity contains dc and multiple even-frequency components whereas the simulation considered only the 2Ω components. Nevertheless, when dc, 2Ω , and 4Ω components of laser intensity are considered in the simulation, we find no significant emergences of other frequency components by the distortion of the ΔT waveforms (see APPENDIX A). The laser irradiation method can steadily and stably modulate the temperature gradient at a frequency of tens of kilohertz, which is applicable to phase-detection techniques for accurately characterizing the magneto-thermoelectric effects.

D. Geometrical correction of the anomalous Nernst effect induced by focused laser beams

Because electromotive forces are generated only in the region irradiated by laser beams, we must correct the generated electric voltages shown in Fig. 4(c) by considering the measurement geometry to calculate the values of Q_{ANE} . The geometrically corrected electric voltage, V'_m , is given by

$$V'_m = \left(\frac{\pi\sigma^2}{2wt_{\text{Co}}} \right) 4\pi M Q_{\text{ANE}} \int_{-(t_{\text{Ru}}+t_{\text{Co}})}^{-t_{\text{Ru}}} dz \nabla T(z). \quad (6)$$

Appendix B provides a detailed derivations of Eq. (6). To confirm the validity of Eq. (6), where V'_m is inversely proportional to w , we fabricated Hall devices with $w = l = 0.10, 0.20, 0.30,$ and 0.40 mm using the Ru(5 nm)/Co(60 nm) bilayer. Figure 6(a) shows V as a function of H at $\varphi = 90^\circ$ and $P = 70$ mW for $w = 0.10, 0.20, 0.30,$ and 0.40 mm. Moreover, the linear dependence of ΔV on $1/w$ shown in Fig 6(b) indicates that Eq. (6) is valid. Notably, Eq. (6) indicates that the electric voltage generated by laser irradiation is optimized when the device size w becomes as large as the spot size σ . Hence, the laser irradiation method can generate detectable electric voltages in micrometer-sized devices by focusing the laser beams, whereas heater methods require a millimeter-sized device owing to the small temperature gradient. The laser irradiation method can expand the range of thermoelectric materials that can be investigated, including micrometer-sized single crystals and cleaved van der Waals layered materials [37–39].

E. Calculation of the coefficient of the anomalous Nernst effect Q_{ANE}

Figure 7 shows the t_{Co} dependence of Q_{ANE} , which was calculated by substituting the characterized values of $4\pi M_s$ [Fig. 3(a)], $V'_m (= \Delta V_{\text{fit}})$ [Fig. 4(c)], and ∇T [Fig. 5(e)] to Eq. (6). The inset of Fig. 7 shows the transverse Seebeck coefficient, S_{xy} . The estimation of Q_{ANE} shown in Fig. 7 ignores the spin Seebeck effect for the small spin Hall angle of Ru [40]. Q_{ANE} increases with a reduction in t_{Co} and is maximized at $t_{\text{Co}} = 7$ nm. Reference [21] reported a similar dependence of Q_{ANE} on the thickness of the ferromagnetic metal. This increasing tendency can be explained by the increasing contribution of impurity scattering or the intrinsic ANE due to the modification of the electronic band structure, based on the Mott relationship [41,42]. In contrast, the reduction in Q_{ANE} at less than 5 nm may be ascribed

to the decrease in the Curie temperature. The values of Q_{ANE} shown in Fig. 7 have the same order of magnitude as those reported in previous studies ranging from 2 to 40 nV K⁻¹ kG⁻¹ [21,43,44]. Furthermore, we measured the ANE at $t_{\text{Co}} = 7$ nm using a conventional method with a heater for comparison (see APPENDIX C). The estimated Q_{ANE} is 22 nV K⁻¹ kG⁻¹ compared with 14 nV K⁻¹ kG⁻¹ in Fig. 6. We observe a systematic error in Q_{ANE} of approximately 40 percent, which is attributed mainly to the selection of material parameters and the lack of consideration of heat conduction in the y -direction. The consistency between the laser irradiation and heater experiments also indicates that the laser irradiation method is usable in the quantitative study of ANE when combined with finite element simulation.

IV. CONCLUSION

We quantitatively studied the thickness dependence of the anomalous Nernst effect induced by laser irradiation in Ru(5 nm)/Co(t_{Co})($t_{\text{Co}} = 3, 5, 7, 10, 20, 40,$ and 60 nm) bilayers. The measured transverse electric voltages and simulated temperature gradients were used to calculate the anomalous Nernst coefficients. The thickness dependence of the anomalous Nernst coefficients quantitatively and qualitatively reproduces those in previous reports and one independently characterized using homogeneous temperature gradients prepared by heaters. This study also highlights that temperature gradients as large as approximately 10³ K/mm can be created by focusing laser beams on a micrometer-sized area while stably modulating the intensity at a frequency of tens of kilohertz. These advantages of the laser irradiation method are beneficial for understanding the physics of the anomalous Nernst effect and exploring novel thermoelectric materials.

ACKNOWLEDGMENTS

We thank Takafumi Obayashi, Tomoya Itoh, and Tetsuma Mandokoro for their technical assistance and Hiro Munekata for his fruitful discussion. This study was partially supported by JSPS KAKENHI (Grant Nos. JP22K14588, JP24K00938, JP23K22425, JP21H01032, JP20H05665, JP24H00007, and JP23H01984), the Frontier Photonic Sciences Project (Grant Nos. JP01212307, and JP01212405), MEXT X-NICS (Grant No. JPJ011438), ASUNARO Grant, JST CREST (Grant No. JPMJCR24R5), and the Collaborative Research Program of the Institute for Chemical Research, Kyoto University.

APPENDIX A: TEMPERATURE MODULATION BY LASER BEAMS WITH DC AND HARMONIC INTENSITY COMPONENTS

In the experimental configuration, the laser intensity included a dc component and even harmonics of 42 kHz, which is the driving frequency of the PEM. We first show the time evolutions of the $P_{2\Omega}$

and $\Delta T'$, a difference between temperatures at the top and bottom of the Co layer, as shown in Fig. 8(a) for $t_{\text{Co}} = 60$ nm at $P_{2\Omega} = 52.1$ mW. Furthermore, when the amplitude ratio of the dc, 2Ω , and 4Ω of the P waveform [Fig 8(b)] is set at 1:0.744:0.232 as in the experiments, we simulated the time evolution of $\Delta T'$. Figure 8(b) shows the time evolutions of P and $\Delta T'$ for $t_{\text{Co}} = 60$ nm at $P = 70$ mW. In this case, the background temperature rises by approximately 10 K. Figure 8(c) indicates the fast Fourier transformation (FFT) of the $\Delta T'$ waveform shown in Fig. 8(b). The ratio of the FFT amplitudes for the dc, 2Ω , and 4Ω components is 1:0.748:0.230, which is identical to the ratio of the laser amplitudes. Therefore, in the frequency range, even when the laser intensity includes the multiple frequency components, we can ignore the appearance of other frequency components in the $\Delta T'$ waveform.

APPENDIX B: DERIVATION OF GEOMETRIC CORRECTION FACTOR

Figure 9(a) shows a schematic of a Hall device illuminated by focused laser beams. For simplicity, we first consider that the spatial intensity profile of laser beams is a top hat distribution with a side length of 2σ . Figure 9(b) shows our model and the equivalent electrical circuit. Along the z -direction, a cuboid including the excited area is divided into n pieces of strip with a size of $2\sigma \times l \times \Delta t$. Here, the fractional resistance, Δr , of each small strip is expressed as follows:

$$\Delta r = \frac{\rho l}{2\sigma \Delta t}. \quad (7)$$

The combined resistance, R' , of the other strips is given by

$$R' = \frac{\Delta r}{n-1} \cong \frac{\Delta r}{n} = \frac{\rho l}{2\sigma t}. \quad (8)$$

The combined resistance, R'' , of the region excluding the cuboid is expressed as

$$R'' = \frac{\rho l}{(w-2\sigma)t}. \quad (9)$$

Therefore, the total resistance, R , of the equivalent circuit becomes

$$R = \Delta r + \frac{R'R''}{R'+R''}. \quad (10)$$

When the electromotive force, ΔV_{ANE} , is generated only in the small strip, the shunt electric current, $\Delta I''$, flowing in the resistance R'' is given by

$$\Delta I'' = \left(\frac{\Delta V_{\text{ANE}}}{R} \right) \left(\frac{R'}{R'+R''} \right) = \frac{R' \Delta V_{\text{ANE}}}{\Delta r R' + R' R'' + \Delta r R''}. \quad (11)$$

Using the superposition theorem [45], the summed electric current, I'' , flowing in the resistance R'' becomes

$$\begin{aligned} I'' &= \sum_{k=1}^n \Delta I''_k \\ &= \frac{2\sigma 4\pi M Q_{\text{ANE}} \sum_{k=1}^n \nabla T_k}{\rho l \left(\frac{1}{2\sigma \Delta t} + \frac{1}{(w-2\sigma)t} + \frac{1}{(w-2\sigma)\Delta t} \right)} \\ &\cong \left(\frac{w-2\sigma}{w} \right) \left(\frac{4\sigma^2}{\rho l} \right) 4\pi M Q_{\text{ANE}} \sum_{k=1}^n \nabla T_k \Delta t, \end{aligned} \quad (12)$$

where ∇T_k is the vertical temperature gradient in a k^{th} strip. Therefore, the measured electric voltage, V_m , is given by

$$V_m = R'' I'' = \left(\frac{4\sigma^2}{wt} \right) 4\pi M Q_{\text{ANE}} \sum_{k=0}^n \nabla T_k \Delta t. \quad (13)$$

Although the above derivation assumes a top hat intensity profile, we employed laser beams with a Gaussian spatial intensity profile in the experiments. Although the amplitude of the vertical

temperature gradients depends on the position of the illuminated region, the laser-induced electric voltage depends linearly on the laser power, and the in-plane temperature gradients are canceled out. Therefore, we can calculate the electric voltages for excitation with a Gaussian laser beam using the following simple transformation. We consider the condition in which the total powers of the Gaussian and top hat beams are identical, as follows:

$$\int_{-\infty}^{\infty} dx \int_{-\infty}^{\infty} dy I e^{-2(x^2+y^2)/\sigma^2} = \int_{-\sigma}^{\sigma} dx \int_{-\sigma}^{\sigma} dy I', \quad (14)$$

where I and I' denote the peak intensity of the Gaussian beam and intensity of the top hat beam, respectively. In this case, the intensity ratio becomes $I : I' = 8 : \pi$. Considering the intensity ratio, the geometrically corrected electric voltage, V'_m , becomes

$$V'_m = \left(\frac{\pi\sigma^2}{2wt} \right) 4\pi M Q_{\text{ANE}} \int_0^t dz \nabla T(z). \quad (15)$$

APPENDIX C: HEATER EXPERIMENT AND CALCULATION OF ANOMALOUS NERNST EFFECT COEFFICIENT

We demonstrate the characterization of the ANE using homogeneous temperature gradients prepared using a heater. The measurement configuration is shown in Fig. 10(a). We cut the Ru(5 nm)/Co (7 nm) film into a piece of 6 mm×3 mm, which was sandwiched between a Peltier heater and a 3-mm-thick AlN block of 5 mm×30 mm. The AlN block was fixed to a heat bath composed of oxygen-free Cu using Mo screws. When the temperature on the top surface of the Peltier heater was set at 60.0°C, the temperature on the top surface of the AlN block was 44.5°C. The temperatures were measured using thermistors. Under these temperature settings, we measured the ANE voltages as a function of the in-plane magnetic field [Fig. 10(b)]. The magnetic hysteresis shows a voltage jump of approximately 13 μV . Assuming that the temperature gradient was linear, we calculated the value of Q_{ANE} to be approximately 22 nV K⁻¹ kG⁻¹ using a temperature gradient of 4.6 K mm⁻¹.

- [1] G. E. W. Bauer, E. Saitoh, and B. J. van Wees, Spin caloritronics, *Nat. Mater.* **11**, 391 (2012).
- [2] H. Yu, S. D. Brechet, and J.-P. Ansermet, Spin caloritronics, origin and outlook, *Phys. Lett. A* **381**, 825 (2017).
- [3] K. Uchida, S. Takahashi, K. Harii, J. Ieda, W. Koshibae, K. Ando, S. Maekawa, and E. Saitoh, Observation of the spin Seebeck effect, *Nature* **455**, 778 (2008).
- [4] M. Mizuguchi, and S. Nakatsuji, Energy-harvesting materials based on the anomalous Nernst effect, *Sci. Technol. Adv. Mater.* **20**, 262 (2019).
- [5] H. Nakayama, K. Masuda, J. Wang, A. Miura, K. Uchida, M. Murata, and Y. Sakuraba, Mechanism of strong enhancement of anomalous Nernst effect in Fe by Ga substitution, *Phys. Rev. Mater.* **3**, 114412 (2019).
- [6] L. Ma, Y. Zhang, H. Zhao, H. R. Fu, M. Tang, H. L. Yang, Z. Shi, N. Tian, and C. Y. You, Anomalous Nernst effect in epitaxial Fe and $\text{Fe}_x\text{Ni}_{1-x}$ alloy thin films, *AIP Adv.* **9**, 035227 (2019).
- [7] T. Seki, Y. Sakuraba, K. Masuda, A. Miura, M. Tsujikawa, K. Uchida, T. Kubota, Y. Miura, M. Shirai, and K. Takanashi, Enhancement of the anomalous Nernst effect in Ni/Pt superlattices, *Phys. Rev. B* **103**, L020402 (2021).
- [8] C. Fang, C. H. Wan, Z. H. Yuan, L. Huang, X. Zhang, H. Wu, Q. T. Zhang, and X. F. Han, Scaling relation between anomalous Nernst and Hall effect in $[\text{Pt}/\text{Co}]_n$ multilayers, *Phys. Rev. B* **93**, 054420 (2016).
- [9] M. Li, H. Pi, Y. Zhao, T. Lin, Q. Zhang, X. Hu, C. Xiong, Z. Qiu, L. Wang, Y. Zhang *et al.*, Large Anomalous Nernst Effects at Room Temperature in Fe_3Pt Thin Films, *Adv. Mater.* **35**, 2301339 (2023).
- [10] M. Ikhlas, T. Tomita, T. Koretsune, M.-T. Suzuki, D. Nishio-Hamane, R. Arita, Y. Otani, and S. Nakatsuji, Large anomalous Nernst effect at room temperature in a chiral antiferromagnet, *Nat. Phys.* **13**, 1085 (2017).
- [11] A. Sakai, Y. P. Mizuta, A. A. Nugroho, R. Sihombing, T. Koretsune, M.-T. Suzuki, N. Takemori, R. Ishii, D. Nishio-Hamane, R. Arita *et al.*, Giant anomalous Nernst effect and quantum-critical scaling in a ferromagnetic semimetal, *Nat. Phys.* **14**, 1119 (2018).
- [12] H. Reichlova, R. Schlitz, S. Beckert, P. Swekis, A. Markou, Y.-C. Chen, D. Kriegner, S. Fabretti, G. H. Park, A. Niemann *et al.*, Large anomalous Nernst effect in thin films of the Weyl semimetal Co_2MnGa , *Appl. Phys. Lett.* **113**, 212405 (2018).
- [13] Y. Pan, C. Le, B. He, S. J. Watzman, M. Yao, J. Gooth, J. P. Heremans, Y. Sun, and C. Felser, Giant anomalous Nernst signal in the antiferromagnet YbMnBi_2 , *Nat. Mater.* **21**, 203 (2022).
- [14] S. Beckert, J. Godinho, F. Johnson, J. Kimák, E. Schmoranzarová, J. Zemen, Z. Šobáň, K. Olejník, J. Železný, J. Wunderlich *et al.*, Anomalous Nernst effect in Mn_3NiN thin films, *Phys. Rev. B* **108**, 024420 (2023).
- [15] T. Asaba, V. Ivanov, S. M. Thomas, S. Y. Savrasov, J. D. Thompson, E. D. Bauer, and F. Ronning,

- Colossal anomalous Nernst effect in a correlated noncentrosymmetric kagome ferromagnet, *Sci. Adv.* **7**, eabf1467 (2021).
- [16] M. Papaj, and L. Fu, Enhanced anomalous Nernst effect in disordered Dirac and Weyl materials, *Phys. Rev. B* **103**, 075424 (2021).
- [17] I. Samathrakris, T. Long, Z. Zhang, H. K. Singh, and H. Zhang, Enhanced anomalous Nernst effects in ferromagnetic materials driven by Weyl nodes, *J. Phys. D: Appl. Phys.* **55**, 074003 (2022).
- [18] T. Yamazaki, T. Seki, R. Modak, K. Nakagawara, T. Hirai, K. Ito, K. Uchida, and K. Takanashi, Thickness dependence of anomalous Hall and Nernst effects in Ni-Fe thin films, *Phys. Rev. B* **105**, 214416 (2022).
- [19] H. Narita, M. Ikhlas, M. Kimata, A. A. Nugroho, S. Nakatsuji, and Y. Otani, Anomalous Nernst effect in a microfabricated thermoelectric element made of chiral antiferromagnet Mn_3Sn , *Appl. Phys. Lett.* **111**, 202404 (2017).
- [20] T. Kikkawa, K. Uchida, S. Daimon, Y. Shiomi, H. Adachi, Z. Qiu, D. Hou, X.-F. Jin, S. Maekawa, and E. Saitoh, Separation of longitudinal spin Seebeck effect from anomalous Nernst effect: Determination of origin of transverse thermoelectric voltage in metal/insulator junctions, *Phys. Rev. B* **88**, 214403 (2013).
- [21] T. C. Chuang, P. L. Su, P. H. Wu, and S. Y. Huang, Enhancement of the anomalous Nernst effect in ferromagnetic thin films, *Phys. Rev. B* **96**, 174406 (2017).
- [22] M. Weiler, M. Althammer, F. D. Czeschka, H. Huebl, M. S. Wagner, M. Opel, I.-M. Imort, G. Reiss, A. Thomas, R. Gross *et al.*, Local Charge and Spin Currents in Magnetothermal Landscapes, *Phys. Rev. Lett.* **108**, 106602 (2012).
- [23] K.-D. Lee, D.-J. Kim, H. Y. Lee, S.-H. Kim, J.-H. Lee, K.-M. Lee, J.-R. Jeong, K.-S. Lee, H.-S. Song, J.-W. Sohn *et al.*, Thermoelectric Signal Enhancement by Reconciling the Spin Seebeck and Anomalous Nernst Effects in Ferromagnet/Non-magnet Multilayers, *Sci. Rep.* **5**, 10249 (2015).
- [24] R. Iguchi, S. Kasai, K. Koshikawa, N. Chinone, S. Suzuki, and K. Uchida, Thermoelectric microscopy of magnetic skyrmions, *Sci. Rep.* **9**, 18443 (2019).
- [25] C. Zhang, J. M. Bartell, J. C. Karsch, I. Gray, and G. D. Fuchs, Nanoscale Magnetization and Current Imaging Using Time-Resolved Scanning-Probe Magnetothermal Microscopy, *Nano Lett.* **21**, 4966 (2021).
- [26] J. M. Bartell, D. H. Ngai, Z. Leng, and G. D. Fuchs, Towards a table-top microscope for nanoscale magnetic imaging using picosecond thermal gradients, *Nat. Commun.* **6**, 8460 (2015).
- [27] F. Johnson, J. Kimák, J. Zemen, Z. Šobáň, E. Schmoranzarová, J. Godinho, P. Němec, S. Beckert, H. Reichlová, D. Boldrin *et al.*, Identifying the octupole antiferromagnetic domain orientation in Mn_3NiN by scanning anomalous Nernst effect microscopy, *Appl. Phys. Lett.* **120**, 232402

(2022).

- [28] A. Pandey, J. Deka, J. Yoon, A. Mathew, C. Koerner, R. Dreyer, J. M. Taylor, S. S. P. Parkin, and G. Woltersdorf, Anomalous Nernst Effect-Based Near-Field Imaging of Magnetic Nanostructures, *ACS Nano* **18**, 31949 (2024).
- [29] A. Yariv and P. Yeh, *Photonics: Optical Electronics in Modern Communications* (Oxford University Press, Oxford, UK, 2007).
- [30] C. Multiphysics, Introduction to COMSOL Multiphysics Version: 6.2, *COMSOL Multiphysics* (Burlington, MA, 1998), accessed 17 December 2024.
- [31] C. Multiphysics, Introduction to the Wave Optics Module Version: 6.2, *COMSOL Multiphysics* (Burlington, MA, 1998), accessed 17 December 2024.
- [32] C. Multiphysics, Introduction to the Heat Transfer Module Version: 6.2, *COMSOL Multiphysics* (Burlington, MA, 1998), accessed 17 December 2024.
- [33] J. M. D. Coey, *Materials for Spin Electronics*, in *Spin Electronics*, edited by M. Ziese and M. J. Thornton (Springer, Berlin, 2001).
- [34] L. Ouarbya, A. J. Tosser, and C. R. Tellier, Effects of electron scatterings on thermal conductivity of thin metal films, *J. Mater. Sci.* **16**, 2287 (1981).
- [35] A. D. Avery, S. J. Mason, D. Bassett, D. Wesenberg, and B. L. Zink, Thermal and electrical conductivity of approximately 100-nm permalloy, Ni, Co, Al, and Cu films and examination of the Wiedemann-Franz Law, *Phys. Rev. B* **92**, 214410 (2015).
- [36] S. Beckert, J. Godinho, F. Johnson, J. Kimák, E. Schmoranzarová, J. Zemen, Z. Šobáň, K. Olejník, J. Železný, J. Wunderlich *et al.*, Anomalous Nernst effect in Mn₃NiN thin films, *Phys. Rev. B* **108**, 024420 (2023).
- [37] M. Ceccardi, A. Zeugner, L. C. Folkers, C. Hess, B. Büchner, D. Marré, A. Isaeva, and F. Caglieris, Anomalous Nernst effect in the topological and magnetic material MnBi₄Te₇, *npj Quantum Mater.* **8**, 76 (2023).
- [38] K. Tang, Y. Yang, J. Shen, M. Shi, N. Zhang, H. Li, H. Li, Z. Liu, D. Shen, R. Wang *et al.*, Unconventional anomalous Hall effect and large anomalous Nernst effect in antiferromagnet SmMnBi₂, *Commun. Mater.* **5**, 89 (2024).
- [39] J. Xu, W. A. Phelan, and C.-L. Chien, Large Anomalous Nernst Effect in a van der Waals Ferromagnet Fe₃GeTe₂, *Nano Lett.* **19**, 8250 (2019).
- [40] H. Yuasa, F. Nakata, R. Nakamura, and Y. Kurokawa, Spin Seebeck coefficient enhancement by using Ta₅₀W₅₀ alloy and YIG/Ru interface, *J. Phys. Appl. Phys.* **51**, 134002 (2018).
- [41] G.-H. Park, H. Reichlova, R. Schlitz, M. Lammel, A. Markou, P. Swekis, P. Ritzinger, D. Kriegner, J. Noky, J. Gayles *et al.*, Thickness dependence of the anomalous Nernst effect and the Mott relation of Weyl semimetal Co₂MnGa thin films, *Phys. Rev. B* **101**, 060406 (2020).
- [42] Y. Pu, D. Chiba, F. Matsukura, H. Ohno, and J. Shi, Mott Relation for Anomalous Hall and

- Nernst Effects in $Ga_{1-x}Mn_xAs$ Ferromagnetic Semiconductors, *Phys. Rev. Lett.* **101**, 117208 (2008).
- [43] J. Weischenberg, F. Freimuth, S. Blügel, and Y. Mokrousov, Scattering-independent anomalous Nernst effect in ferromagnets, *Phys. Rev. B* **87**, 060406 (2013).
- [44] D. Yang, L. Yi, S. Fan, X. He, Y. Xu, M. Liu, L. Ding, L. Pan, and J. Q. Xiao, Spin Seebeck coefficients of Fe, Co, Ni, and $Ni_{80}Fe_{20}$ 3d-metallic thin films, *Mater. Res. Bull.* **136**, 111153 (2021).
- [45] J. D. Irwin and R. M. Nelms, *Basic Engineering Circuit Analysis*, 12th ed. (Wiley Publishing, New Jersey, 2020)
- [46] J. R. Rumble, *CRC Handbook of Chemistry and Physics*, 104th ed. (CRC Press, Boca Raton, 2023).
- [47] I. D. Marinescu, T. Doi, and E. Uhlmann, *Handbook of Ceramics Grinding and Polishing*, 2nd ed. (William Andrew, Norwich, 2015).
- [48] D. A. Ditmars, S. Ishihara, S. S. Chang, G. Bernstein, and E. D. West, Enthalpy and Heat-Capacity Standard Reference Material: Synthetic Sapphire (α - Al_2O_3) from 10 to 2250 K, *J. Res. J. Res. Natl. Bur. Stand.* **87**, 159-163 (1982).
- [49] G. M. Katyba, K. I. Zaytsev, I. N. Dolganova, I. A. Shikunova, N. V. Chernomyrdin, S. O. Yurchenko, G. A. Komandin, I. V. Reshetov, V. V. Nesvizhevsky, and V. N. Kurlov, Sapphire shaped crystals for waveguiding, sensing and exposure applications, *Prog. Cryst. Growth Charact. Mater.* **64**, 133 (2018).

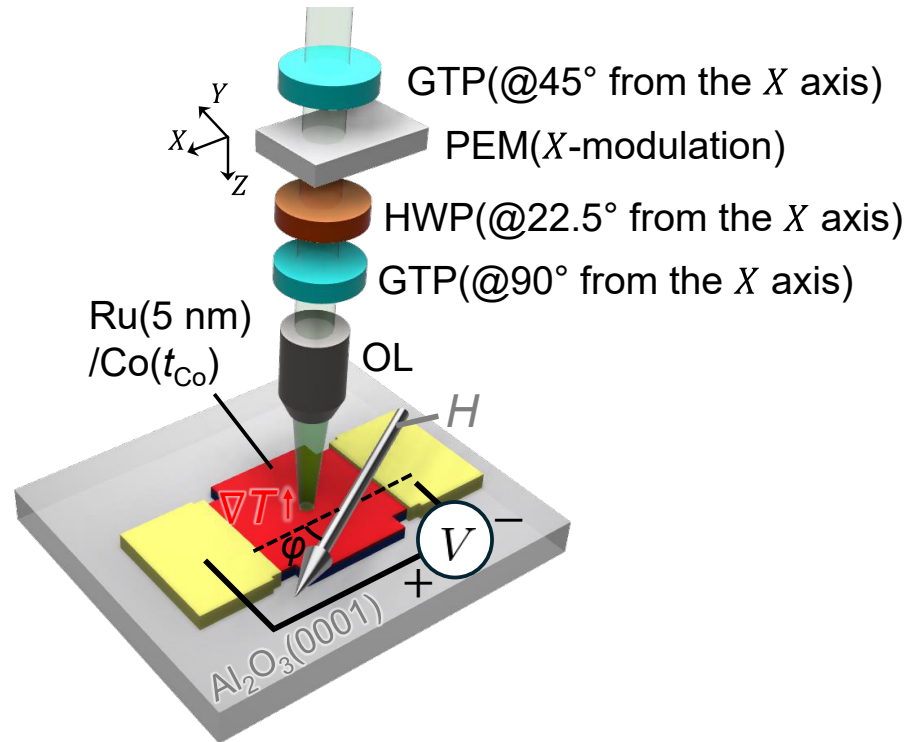


FIG. 1. Schematic of the experimental set-up. The intensity-modulated laser beams are focused on the center of the Hall cross, forming temperature gradients, ∇T , along the thickness direction. In-plane magnetic field, H , is applied at an angle of ϕ from the X axis. Abbreviations: GTP (Glan Taylor prism), PEM (Photo-elastic modulator), HWP (Half-wave plate), and OL (Objective lens).

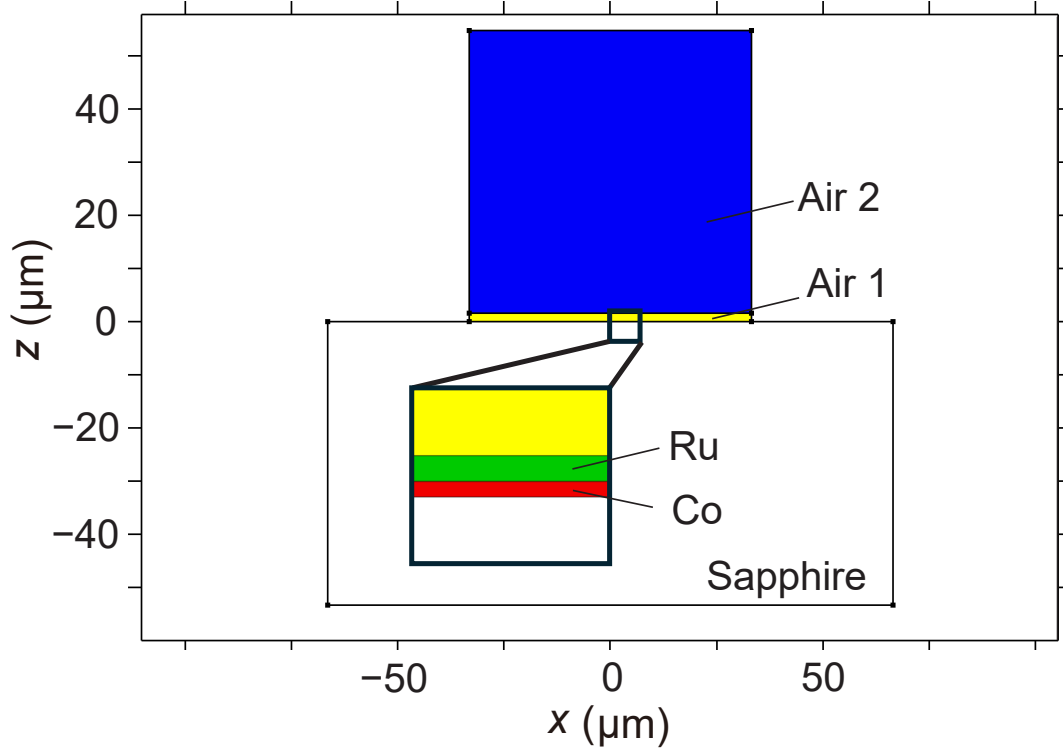


FIG. 2. Model for the finite element simulation. We set the layer sizes of the substrate (white), Co (red), Ru (green), air 1 (yellow), and air 2 (blue) layers at $x \times y \times z = 106.4 \mu\text{m} \times 30 \mu\text{m} \times 53.2 \mu\text{m}$, $106.4 \mu\text{m} \times 30 \mu\text{m} \times t_{\text{Co}}$, $106.4 \mu\text{m} \times 30 \mu\text{m} \times 5 \text{ nm}$, $53.2 \mu\text{m} \times 30 \mu\text{m} \times 1.6 \mu\text{m}$, and $53.2 \mu\text{m} \times 30 \mu\text{m} \times 53.2 \mu\text{m}$, respectively. For the simulation of the temperature profile, each layer was divided into a mesh. The x and z mesh sizes of the substrate, Co/Ru, air 1, and air 2 layers were $5.32 \mu\text{m} \times 90 \text{ nm}$, $5.32 \mu\text{m} \times 0.5 \text{ nm}$, $5.32 \mu\text{m} \times 16 \text{ nm}$, and $5.32 \mu\text{m} \times 532 \text{ nm}$, respectively. To reduce the computational cost and time, mesh division was not applied along the y -direction, i.e., 2D simulation.

TABLE 1. Material parameters used in the finite element simulations. The densities, and heat capacities of Ru and Co and refractive indexes at $\lambda = 532$ nm of Ru, Co, and sapphire are cited from ref. [46]. The thermal conductivities of Ru and Co are calculated from the measured resistivity based on Wiedemann-Franz’s law. The density, heat capacity, and thermal conductivity of sapphire are cited from refs. [47–49], respectively.

Material	Refractive index	Density [g cm ⁻³]	Heat Capacity [J kg ⁻¹ K ⁻¹]	Thermal Conductivity [W m ⁻¹ K ⁻¹]
Ru	$3.1 - 4.7i$	12.4	238	14.3
Co	$2.0 - 3.6i$	8.9	431	18.1
Sapphire	1.77	4.0	750	41.9

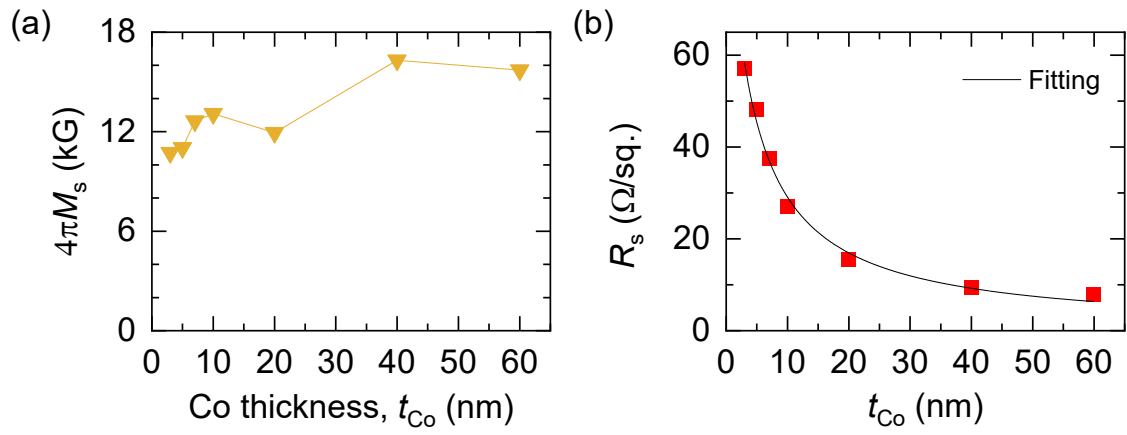


FIG. 3. Co thickness, t_{Co} , dependence of (a) saturation magnetization, $4\pi M_s$, and (b) sheet resistance, R_s . The fitting result with Eq. (5) is indicated by a solid black line.

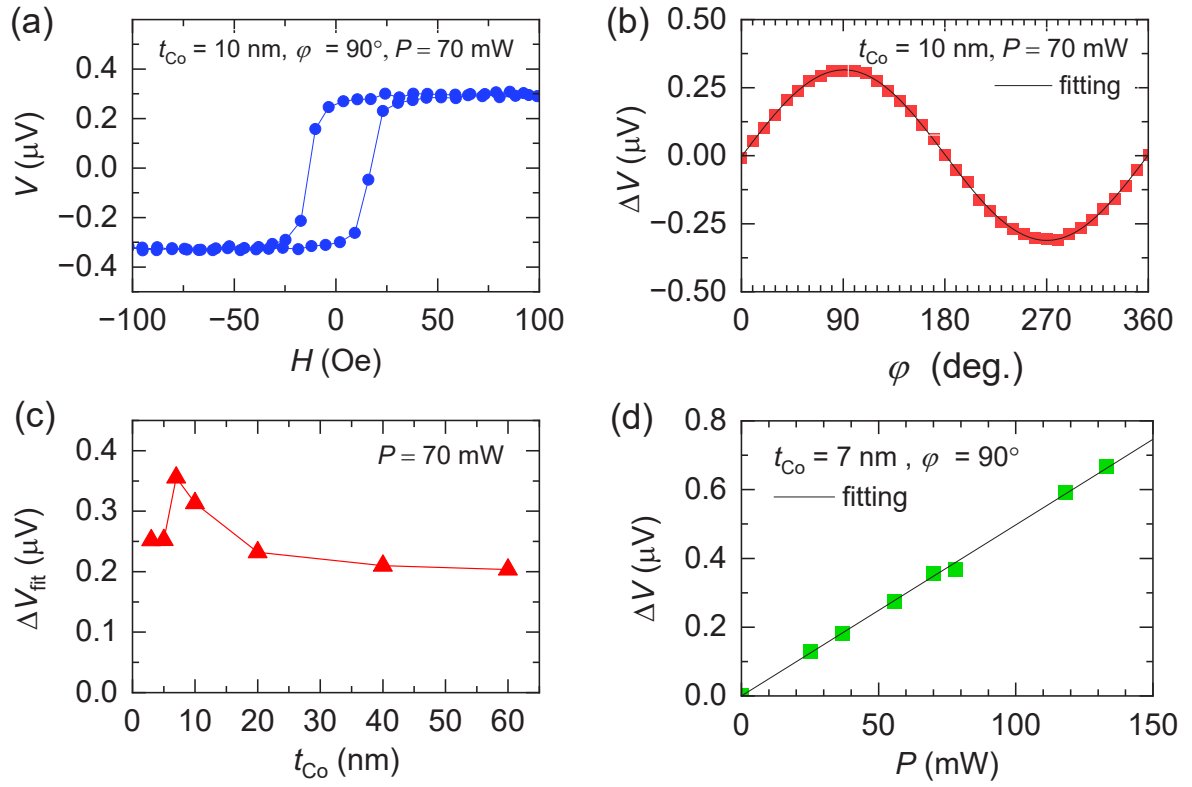


FIG. 4. Anomalous Nernst effect (ANE) induced by laser irradiation. (a) Magnetic hysteresis of electric voltages, V , measured for $t_{\text{Co}} = 10$ nm at $\varphi = 90^\circ$ and an average laser power, P , of 70 mW. (b) φ dependence of voltage jump, ΔV , for $t_{\text{Co}} = 10$ nm at $P = 70$ mW. The φ dependence at each t_{Co} is fitted with a sine function $\Delta V_{\text{fit}} \sin \varphi$. (c) t_{Co} dependence of ΔV_{fit} at $P = 70$ mW. (d) P dependence of ΔV for $t_{\text{Co}} = 7$ nm at $\varphi = 90^\circ$. We add a linear-fitting line to Fig. 4(d).

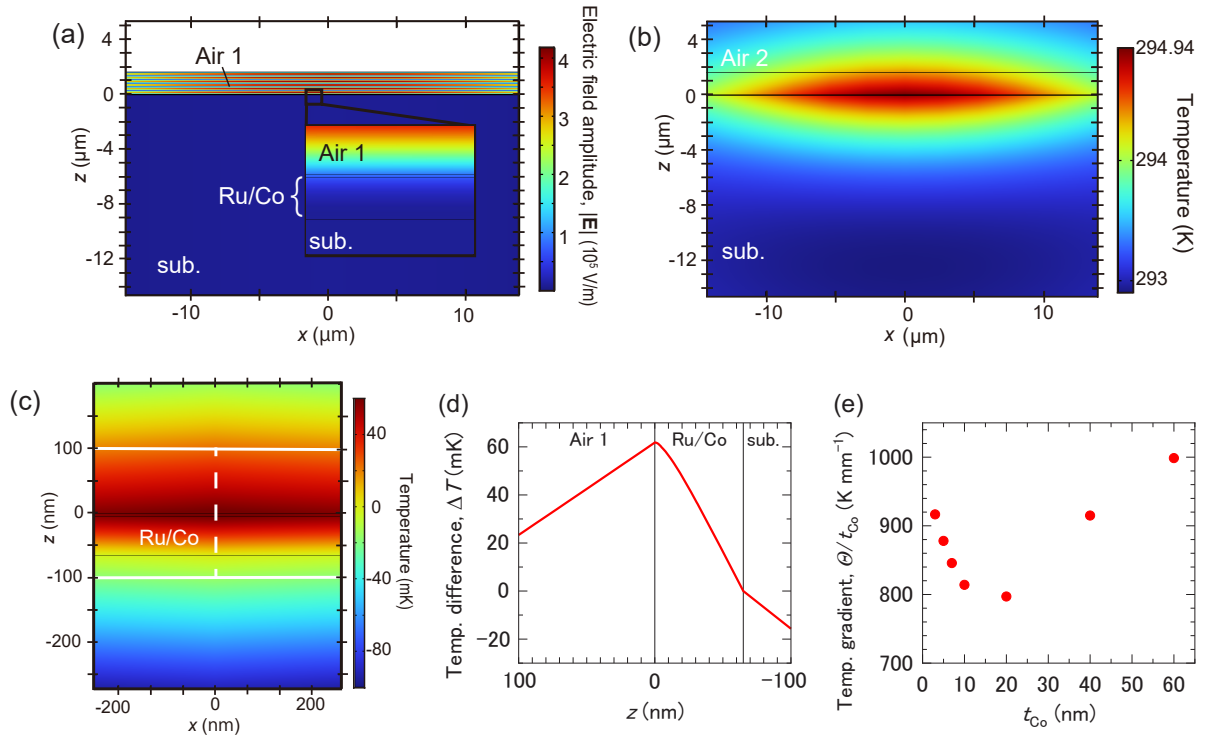


FIG. 5. Finite element simulations of light electric field and temperature. (a) Spatial profiles of light electric-field amplitude, $|\mathbf{E}|$, for $t_{\text{Co}} = 60$ nm. (b) Spatial profile and (c) magnified view of temperature for $t_{\text{Co}} = 60$ nm when the temperature is maximized. The color scale shows the temperature variation from the surface of the Ru. A cut line is indicated by a white broken line. (d) Temperature difference, ΔT , from the air1/Ru interface along the cut line. (e) t_{Co} dependence of the integral of temperature gradients along the Co thickness, Θ , normalized by t_{Co} . Throughout the finite element simulations, we set the average power of the 2Ω component at $P_{2\Omega} = 52.1$ mW.

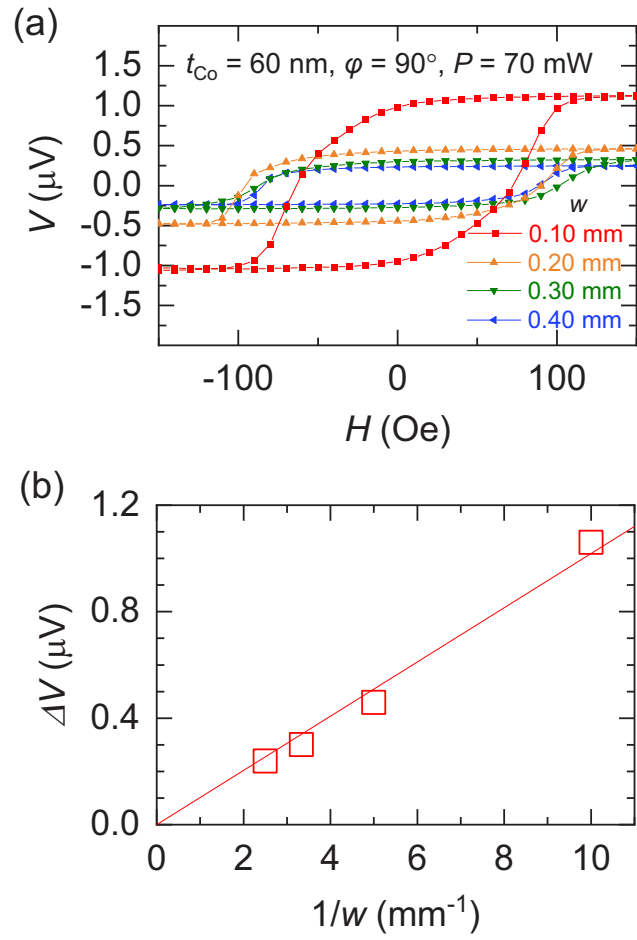


FIG. 6. Device-size dependence of ANE voltages. (a) Magnetic hysteresis of V measured for $t_{\text{Co}} = 60 \text{ nm}$ at $\varphi = 90^\circ$ and $P = 70 \text{ mW}$. (b) Device-width dependence of ΔV for $t_{\text{Co}} = 60 \text{ nm}$ at $\varphi = 90^\circ$. The solid line indicates the linear fitting.

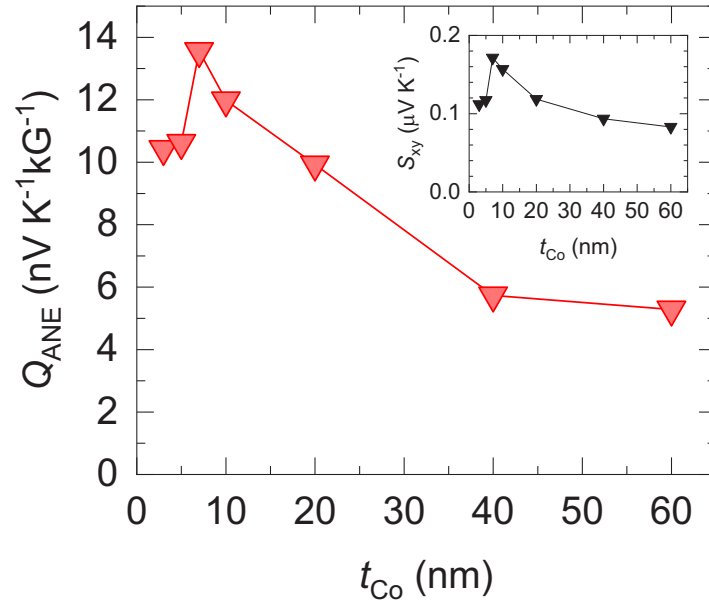


FIG. 7. t_{Co} dependence of ANE coefficient, Q_{ANE} . The inset indicates the transverse Seebeck coefficient, S_{xy} , as a function of t_{Co} .

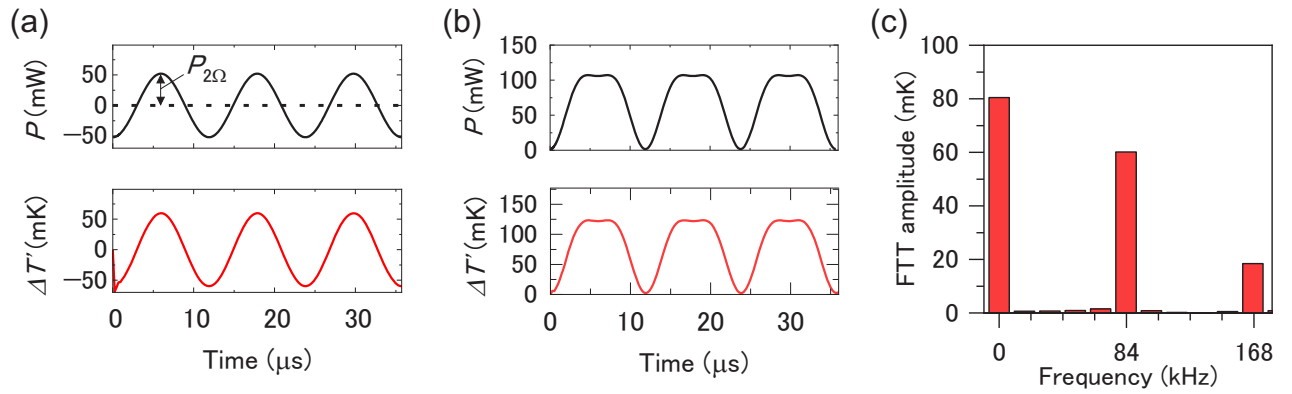


FIG. 8. Time evolution of temperature difference, ΔT , for $t_{\text{Co}} = 60$ nm when the laser beam includes (a) 2Ω amplitude component and (b) dc, 2Ω , and 4Ω amplitude components. Here, the ΔT is a difference between temperatures of the surface and bottom surface of the Co layer. (c) Amplitude of fast Fourier transformation (FFT) of the ΔT waveform.

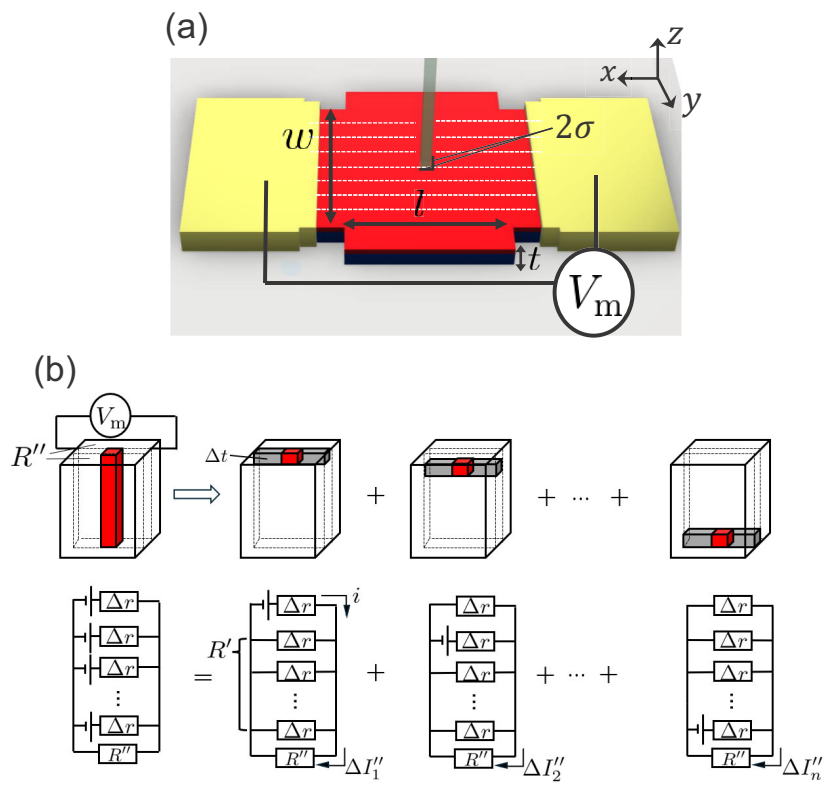


FIG. 9. (a) Schematic illustration for calculating geometrical correction factor. A laser beam, of which the spatial intensity profile is square with a side length of 2σ is focused on the center of a Hall cross with a size of $w \times l$. (b) Equivalent circuit model of ANE induced by local laser heating.

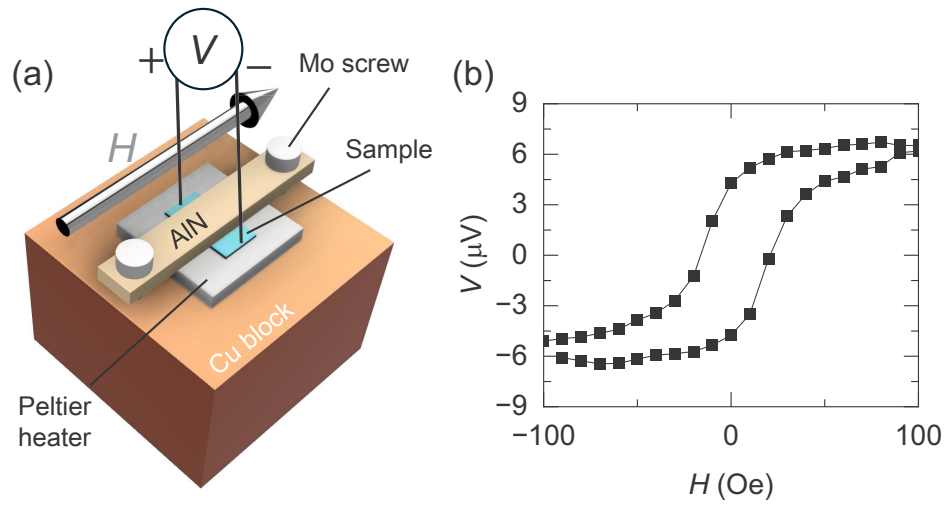


FIG. 10. Characterization of ANE using homogeneous temperature gradients prepared by a heater. (a) Schematic illustration of experimental configuration. (b) Magnetic hysteresis of electric voltage, V , for $t_{\text{Co}} = 7$ nm. Here, we set the surface temperature of the Peltier heat at 60°C , when the surface temperature of the AlN block was 44.5°C .